Adversarial learning for beamforming domain transfer in ultrasound medical imaging

Ultrasonics 156 (2025) 107749

Contents lists available at ScienceDirect

Ultrasonics

journal homepage: www.elsevier.com/locate/ultras

Adversarial learning for beamforming domain transfer in ultrasound medical imaging

Silvia Seoni [a], Massimo Salvi [a], Giulia Matrone [b], Francesco Lapia [c], Chiara Busso [d], Marco A. Minetto [d], Kristen M. Meiburger [a,*]

[a] Biolab, PoliTo^{BIO}Med Lab, Department of Electronics and Telecommunications, Politecnico di Torino, Corso Duca degli Abruzzi 24, 10129 Turin, Italy
[b] Department of Electrical, Computer and Biomedical Engineering, University of Pavia, via Ferrata 5, 27100 Pavia, Italy
[c] ASST Ovest Milanese, Ospedale Nuovo di Legnano, Via Papa Giovanni Paolo II, 20025, Legnano, Milan, Italy
[d] Division of Physical Medicine and Rehabilitation, Department of Surgical Sciences, University of Turin, Corso Dogliotti 14, 10126 Torino, Italy

ARTICLE INFO

Keywords:
Generative adversarial network
Ultrasound image enhancement
Beamforming methods
Delay and sum
Filtered delay multiply and sum
Plane wave imaging

ABSTRACT

Beamforming, the process of reconstructing B-mode images from raw radiofrequency (RF) data, significantly influences ultrasound image quality. While advanced beamforming methods aim to enhance the traditional Delay and Sum (DAS) technique, they require access to raw RF data, which is often unavailable to researchers when using clinical ultrasound scanners. Given that Filtered Delay Multiply and Sum (F-DMAS) is known to provide superior image quality compared to conventional DAS, this study introduces the idea of employing generative adversarial networks (GANs) that transform plane wave DAS images into ones resembling those produced by F-DMAS. We validated the adversarial approach employing three different architectures (traditional Pix2Pix, Pyramidal Pix2Pix and CycleGAN) using full-reference metrics: Root Mean Square Error (RMSE) and Peak Signal-to-Noise Ratio (PSNR). We further propose employing a texture analysis to validate consistency between the generated images and target images, using 27 first-order and second-order parameters; contrast enhancement was evaluated using the Contrast Improvement Index (CII), and clinical relevance was determined through expert qualitative evaluation. The adversarial methods were also compared with traditional image enhancement methods, such as contrast limited adaptive histogram equalization (CLAHE) and histogram matching. The image similarity metrics between all methods were comparable, with the Pyramidal Pix2Pix GAN method showing the best values compared to traditional techniques and other generative models (PSNR = 18.0 ± 0.6 dB, RMSE = 0.126 ± 0.008). The texture features proved to be a clear discriminant between traditional methods and generative models, with values much closer to the target F-DMAS image for the generative models. All employed methods showed an improved contrast over original PW DAS images. A clinical evaluation was then employed to assess the contribution of the generated images compared to the original ones and to distinguish which generative model provided the best qualitative images. The proposed generative adversarial approach proves to be a viable option for enhancing B-mode ultrasound images when there is no access to raw RF data and demonstrates how texture features can be employed to validate deep learning generative models.

1. Introduction

Ultrasound is one of the most widely used imaging methods in the clinical field [1,2]. Because it is non-invasive, inexpensive, and simple to perform, it is often one of the first examinations for the diagnosis of many types of pathologies. A critical factor influencing ultrasound's diagnostic value is the quality of the acquired images. Ultrasound imaging is heavily operator-dependent and multiple elements impact ultrasound image quality, including the acquisition method, probe specifications, display parameters, and presence of noise [3,4]. A key operator-independent determinant of image quality is the beamforming algorithm that is employed to reconstruct the image, which converts raw radiofrequency (RF) signals from the ultrasound probe into final 8-bit B-mode images.

The conventional Delay and Sum (DAS) beamformer adjusts time delays before summing signals and is computationally very simple and

* Corresponding author.
E-mail address: kristen.meiburger@polito.it (K.M. Meiburger).

https://doi.org/10.1016/j.ultras.2025.107749
Received 19 January 2025; Received in revised form 26 May 2025; Accepted 3 July 2025
Available online 9 July 2025

fast. While typically the preferred method for clinical scanners, DAS has some inherent limitations like lower lateral resolution and contrast when in presence of side lobes or reverberation noise [5]. This has motivated research into more advanced beamformers like Filtered Delay Multiply and Sum (F-DMAS), which applies spatial cross-correlation and filtering to enhance image features [5]. Other beamforming methods based on DAS include multiplying the DAS signal with a coherence factor, such as Coherence Factor (CF) [6], Generalized CF (GCF) [7], and Phase and Sign CF (PCF and SCF, respectively) [8]. The Minimum Variance (MV) method dynamically adjusts apodization and steering weights based on raw data, enhancing image quality but increasing computational cost and time for weight estimation compared to DAS [9]. Short-Lag Spatial Coherence (SLSC) beamforming improves image contrast and reduces speckle by leveraging the spatial coherence of backscattered signals over short lags [10]. A common denominator among all beamforming algorithms is the requirement to have access to the raw RF data.

Today, texture analysis is increasingly used as a quantitative tool to characterize the effects of image formation processes, independently of its clinical interpretation [11]. The beamforming algorithm that is employed to reconstruct the image hence modifies the obtained image in terms of contrast and resolution, and also in terms of texture. Texture analysis of B-mode images allows for the extraction of quantitative information on the distribution of pixels and their intensity [11], and has been employed in numerous clinical studies for the assessment of various kinds of tissue, such as muscle [12], liver [13], breast [14], or pathologies such as cardiac disease [15]. A few recent studies have also examined how the image formation process and ultrasound settings, like the dynamic range (dR) value, influence texture parameters [16]. In our previous study [17], we analyzed the effects of beamforming, dynamic range value, and selection of the region of interest on texture parameter analysis in muscular images and phantom images acquired with two different devices, showing that texture metrics are relatively robust across a range of dR values and can be used to differentiate images reconstructed using different beamforming techniques.

In recent years, several deep learning (DL) models have been developed for image reconstruction and enhancement due to some key advantages over traditional beamforming methods [18–22]. These include both generative models, such as GANs, and more conventional architectures, such as convolutional or fully connected networks. Table 1 reports some of the main deep learning models used for ultrasound image enhancement and reconstruction found in the literature, and should not be considered as an exhaustive list. These models demonstrate significant benefits, particularly in terms of inference speed, enabling real-time clinical applications, as well as in their ability to improve image resolution and reduce artifacts. However, a major limitation of DL models is their dependence on large training datasets, which are often difficult to obtain and frequently require access to raw RF data. As a result, many models rely on simulated data, which may limit their generalizability to real-world clinical images [20]. Overall, the current works typically either (1) require raw RF data in input for image reconstruction tasks or (2) use pixel-based input for image enhancement denoising purposes. A few works, such as [23], attempt enhancement directly from standard B-mode images using conventional DL approaches.

This work introduces an innovative application of DL for generating high-quality ultrasound images by transferring beamforming information from pixel-based data, particularly in situations where raw data is not accessible. While the use of GANs for style transfer has been explored in various fields, this work focuses on applying GANs to the enhancement of ultrasound images, specifically by transforming traditional DAS images into images resembling those produced by F-DMAS. In our previous work [24], we demonstrated initial results using a GAN for beamforming domain transfer with a limited dataset. In this study, we extend this research by refining the GAN architectures, improving generalizability across different anatomical structures, and providing a more comprehensive validation of the method using various metrics, including texture parameters and clinical relevance. The main contributions of this work are listed as follows:

– Development of a generative adversarial approach for ultrasound image enhancement through beamforming domain transfer,

Table 1
Representative list of the main deep learning approaches for ultrasound image enhancement and reconstruction.

Authors, years	Task	Input type	Data type	Finding
Nair et al. [23]	Beamforming	Raw data	Field II simulated data and test with phantom images	A DNN model that performs beamforming from raw channel data and jointly generates both a B-mode image and a segmentation map.
He et al. [25]	Image quality Enhancement	Low resolution images	3D Transrectal ultrasound images	A GAN framework to reconstruct high-resolution ultrasound images
Escobar et al. [26]	Image quality Enhancement	Low quality image	Cardiac acquisitions	UltraGAN for ultrasound image enhancement
Zhou et al. [27]	Image quality Enhancement	Low-quality ultrasound images scanned by portable devices	Simulated, phantom and in-vivo data (Carotid and thyroid image)	An advanced two-stage GAN method for enhancing image quality in hand-held ultrasound devices
Zhou et al. [28]	Image quality Enhancement	Raw data	RF signals by scanning the carotid artery, thyroid and radio-carpal joint of 20 healthy volunteers.	The MC-HGAN method to generate high-quality ultrasound images that emulate the MV beamforming method.
Khor et al. [29]	Image quality Enhancement	Low quality image	Simulated, phantom and in-vivo data	A novel wavelet-based GAN for real-time speckle noise reduction in ultrasound images.
Seoni et al. [24]	Image quality Enhancement	Plane wave DAS images	In-vivo images: musculoskeletal and carotid images	GAN to generate B-mode images that emulate focused F-DMAS images from DAS PW images.
Bosco et al. [30]	Image quality Enhancement	Low quality image (SAF)	Field II simulated images for training, phantom and in-vivo images for testing	A U-Net-based GAN to enhance contrast in ultrasound images obtained in a monostatic SA imaging configuration
Cho et al. [31]	Beamforming	Raw data	Open in-vitro and in-vivo data (CUBDL and PICMUS) [31,32]	Deep coherence learning, based on a unsupervised deep learning approach for high-quality PW imaging
Xiao e Yu [33]	Beamforming	Raw data	In-vivo data (musculoskeletal)	A Beamforming-integrated neural network (BINN) that embeds DAS as a sparse matrix beamforming layer
Our GAN approach	Image quality Enhancement	DAS image	In-vivo data (different tissues)	GAN model to generate high-quality B-mode images similar to the focused F-DMAS reconstruction, starting from plane wave DAS images.

GAN: Generative Adversarial Network, MV: Minimum Variance. DAS: Delay and Sum, F-DMAS: Filtered Daly Multiply and Sum, SAF: Monostatic Synthetic Aperture Focusing.

enabling the generation of high-quality B-mode images that mimic focused mode acquisition and F-DMAS reconstruction from single plane-wave (PW) DAS B-mode images without requiring access to raw RF data;
- Investigation and comparison of three different GAN architectures (traditional Pix2Pix, Pyramidal Pix2Pix and CycleGAN) for ultrasound image enhancement, demonstrating their respective strengths and limitations;
- Comprehensive validation framework combining full-reference metrics, texture analysis, contrast evaluation, and qualitative specialist review, revealing how different evaluation approaches capture distinct aspects of image quality;
- Comparative analysis demonstrating the advantages of generative approaches over traditional contrast enhancement methods, with particular focus on texture preservation and clinical applicability.

2. Methods

Our proposed approach introduces a generative adversarial network approach that performs beamforming domain transfer from PW DAS images to focused F-DMAS images without requiring access to raw RF data. Moreover, the proposed approach also optimizes the image dynamic range [34], an often-overlooked parameter that is crucial for final B-mode image generation.

2.1. Dataset

The dataset comprised 980 images obtained from 14 healthy volunteers, following approval of the study protocol by the Local Ethics Committee (n. 24780/2022, approval issued on 19/07/2022). All acquisitions were carried out in accordance with relevant guidelines and regulations, including the Declaration of Helsinki. All participants provided informed consent before data collection. Acquisitions included five musculoskeletal sites: gastrocnemius lateralis, gastrocnemius medialis, vastus lateralis, vastus medialis, and biceps. Carotid artery images were captured in transverse and longitudinal views bilaterally.

For each anatomical site, RF data were collected using both PW and focused transmitting sequences. Images were acquired using the Verasonics Vantage™ Research Ultrasound System (USA), equipped with an L11-5v linear array probe consisting of 128 elements. The system operated at a central frequency of 7.8 MHz, with a sampling frequency of 31 MHz. A 2-cycle sinusoidal burst was employed in transmission. For the plane wave acquisitions, all 128 elements were employed for both transmission and reception, considering a single plane-wave with 0° steering. For focused imaging, the focal depth was set to 30 mm for musculoskeletal tissues and 15 mm for the carotid artery. Thirty-two elements were employed to focus the beam on transmission, resulting in a F# equal to 3.1 and 1.6, respectively. All 128 elements were used in reception. The UltraSound ToolBox was used to beamform the RF data with DAS for PW images and F-DMAS for focused images [35]. A proper equivalent sampling frequency compatible with the second harmonics generation and filtering for the F-DMAS algorithm was considered using USTB for signal beamforming.

After beamforming, envelope detection was applied to the beamformed signals, and images were then log-compressed. Five dynamic range values (50, 55, 60, 65, and 70 dB) were applied to reconstruct the final PW DAS B-mode images. An optimized automatic dR was instead used for focused F-DMAS images [34]. Specifically, the optimal dR is automatically determined by analyzing the histogram of the beamformed log compressed values and calculating a weighted mean of the values to determine the optimal lower limit (e.g., −50, −55, −60, −65, −70 dB). The upper limit was always kept equal to 0 dB. This automatic adjustment allows for more effective utilization of the available intensity range, improving the image quality and ensuring better visualization. This experimental design enables our model to learn both beamforming domain transfer and dynamic range optimization simultaneously. The image dB values were then thresholded considering the selected dR, in the range [-dR; 0 dB] (i.e. all values lower than –dR were set equal to –dR), and were then converted in the range 0–255 to obtain a 8-bit gray level image. The images were interpolated to have a pixel size of 0.055 mm in both axial and lateral directions, ensuring that the final pixel dimensions were consistent with those obtained with common clinical scanners. Specifically, musculoskeletal images were resized to 890 × 692 pixels (50 × 38 mm) and vascular images to 527 × 692 pixels (30 × 38 mm). Finally, all images were automatically cropped to a standardized size of 512 × 512 pixels. Fig. 1 shows examples of carotid and musculoskeletal images. The proposed model was trained on 840 ultrasound images and tested on 140 separate images (50 % from female patients). To create non-overlapping training and test sets, we partitioned the data at the patient level to prevent potential bias between different sets (Table 2).

2.2. Generative models

We investigated three different GAN architectures: traditional Pix2Pix, CycleGAN, and Pyramidal Pix2Pix. The Pix2Pix and Pyramidal Pix2Pix models were trained using paired PW DAS and focused F-DMAS images, as these architectures require one-to-one image correspondences. In contrast, CycleGAN was implemented for its ability to perform unpaired image translation between the DAS and F-DMAS domains.

2.2.1. Traditional Pix2Pix GAN

The traditional Pix2Pix architecture employs a conditional GAN framework for paired image-to-image translation [36]. The generator uses a U-Net architecture, while the discriminator follows a PatchGAN design that classifies NxN image patches as real or fake. The objective function for Pix2Pix combines an adversarial loss with an $L1$ distance loss:

$$L_{pix2pix}(G,D) = L_{GAN}(G,D) + \lambda L1(G) \tag{1}$$

where L_{GAN} represents the adversarial loss and $L1(G)$ represents the $L1$ distance between the generated image $G(x)$ and the target image y, calculated as:

$$L1(G) = E_{x,y}\left[\|y - G(x)\|_1\right] \tag{2}$$

Here, x is the input PW DAS image, y is the corresponding target focused F-DMAS image, and $||\cdot||_1$ denotes the $L1$ norm.

2.2.2. CycleGAN

CycleGAN enables unpaired image translation through cycle consistency [37]. It employs two generator-discriminator pairs (G, D_Y) and (F, D_X) to learn mappings G: X → Y and F: Y → X between DAS (X) and F-DMAS (Y) domains. The objective combines adversarial and cycle consistency losses:

$$L_{cycle}\left(G,F,D_X,D_Y\right) = L_{GAN}(G,D_Y) + L_{GAN}(F,D_X) + \lambda_{cycle}(L_{cycle}(G,F)) \tag{3}$$

where:

$$L_{GAN}(G,D_Y) = E_y[logD_Y(y)\,] + E_x[log(1 - D_Y(G(x)))]$$

$$L_{GAN}(F,D_X) = E_x[logD_X(x)] + E_y[log(1 - D_X(F(y)))]$$

$$L_{cycle}(G,F) = E_x[\|F(G(x)) - x\|_1] + E_y[\|G(F(y)) - y\|_1] \tag{4}$$

L_cycle enforces $F(G(x)) \approx x$ and $G(F(y)) \approx y$ for cycle consistency.

2.2.3. Pyramidal Pix2Pix GAN

The Pyramidal Pix2Pix architecture leverages a multi-resolution design for enhanced image generation [38]. The generator uses an Attention-UNet architecture with self-attention mechanisms to capture long-range dependencies and better preserve global image structure.

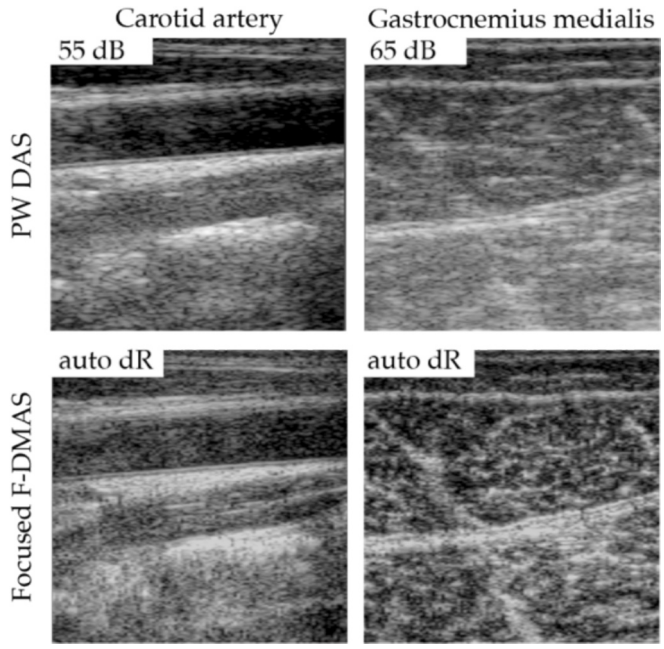

Fig. 1. Examples of carotid and musculoskeletal ultrasound images. The first row presents DAS PW images with two exemplary dynamic range values of 55 dB and 65 dB, while the second row displays the corresponding focused images reconstructed using the F-DMAS method, with the dynamic range (dR) automatically estimated.

Table 2
Dimension of the training and test set.

	Training set	Test set
Carotid images	240	40
Longitudinal Carotid	120	20
Transversal Carotid	120	20
Musculoskeletal Images	600	100
Vastus lateralis	120	20
Vastus medialis	120	20
Gastrocnemius lateralis	120	20
Gastrocnemius medialis	120	20
Biceps	120	20
Total	840	140

Unlike the original implementation that uses three downsampling steps, we modified the architecture to use a single downsampling step, which proved more effective for ultrasound images.

The generator produces multi-resolution outputs, maintaining both fine details and overall characteristics (Fig. 2). The discriminator employs a patch-based approach, particularly effective for texture-based ultrasound images. The loss function incorporates three components:

An adversarial loss to align the distributions of real and generated images;
A full-resolution L1 pixel loss, weighted by 25, to ensure pixel-level accuracy;
An L2 representation matching loss weighted by 25 to match discriminator features, promoting perceptual similarity.

The overall objective function of Pyramidal GAN is defined as:

$$L_{Pyr}(G,D) = L_{GAN}(G,D) + \lambda_1 L_1(G) + \lambda_2 L_2(G) \quad (5)$$

where:

$$L_{GAN}(G,D) = E_y[logD(y)] + E_x[\log(1 - D(G(x)))]$$

$$L1(G) = E_{\{x,y\}}\left[\|y - G(x)\|_1\right]$$

$$L2(G) = E_{\{x,y\}}\left[\|D_{feat}(y) - D_{feat}(G(x))\|_2^2\right] \quad (6)$$

L_{GAN} is the adversarial loss, L_1 is the pixel-wise loss, and L_2 is the feature matching loss. The λ terms are the respective weighting factors. This multi-scale adversarial training framework, combined with our custom loss function, facilitates the synthesis of highly realistic ultrasound images that closely mimic the characteristics of F-DMAS beamforming.

2.2.4. Training details

All models were trained for 200 epochs with alternating generator and discriminator updates. The input size was set to 512x512 pixel and generator weights were saved every 10 epochs, using instance normalization. The best epoch was chosen based on the loss value. The model was trained on a workstation equipped with an Intel Core i9-14900KF CPU, 128 GB of RAM, and an NVIDIA RTX A6000 GPU. The inference time (i.e. the time required to generate the synthetic image from the PW DAS image) is approximately 30 ms.

2.3. Validation

To comprehensively validate the proposed GAN approach, we employed four complementary analysis techniques: 1) full-reference similarity metrics (PSNR and RMSE) to assess pixel-wise fidelity to the F-DMAS images; 2) texture feature analysis to quantitatively compare structural characteristics between generated and reference images; 3) contrast improvement index calculations to measure enhancement, and 4) qualitative specialist evaluation of image quality. These methods aimed to demonstrate the generative model's ability to emulate the texture, contrast, and visual quality of F-DMAS beamforming outputs starting from basic PW DAS images.

Since the proposed method is designed to perform a beamforming domain transfer, we selected F-DMAS as the target image domain due to its well-established capability to enhance both lateral resolution and contrast. However, F-DMAS inherently requires access to RF data, which is often unavailable with commercial clinical scanners. The GAN-based approach aims to bridge this gap by learning a transformation that mimics F-DMAS image quality directly from reconstructed pixel-based B-mode images, without requiring raw RF signals.

To ensure that the adversarial learning approach provides a distinct advantage to traditional contrast enhancement methods, we quantitatively compared the GAN results with two traditional contrast enhancement methods: the contrast limited adaptive histogram equalization (CLAHE) [39] which does not require a target image, and a simple histogram matching technique, using the PW DAS image in input and the F-DMAS optimized image as the target histogram [40].

The three quantitative validation methods that are described in the following three sections were hence employed for all six analyzed methods and are herein referred to with the acronym in parenthesis: the initial PW DAS image (DAS), the CLAHE-enhanced DAS image (CLAHE), the histogram-matched DAS image (HM), the standard Pix2Pix GAN output image (Pix2Pix), the CycleGAN output image (Cycle), and the Pyramidal GAN output image (Pyramidal).

2.3.1. Full reference metrics for image similarity

We computed two full-reference metrics, i.e. the root mean square error (RMSE) [41] and peak signal-to-noise ratio (PSNR)[42], to quantitatively assess pixel-level similarity between the generated images and the target image. Lower RMSE values indicate a smaller average difference from the reference image, while higher PSNR values reflect higher image similarity in terms of reconstruction fidelity. In this work, the reference image is always the F-DMAS output, and these two metrics were calculated for all six methods under comparison. To account for the scale invariance of ultrasound images, we also report RMSE values

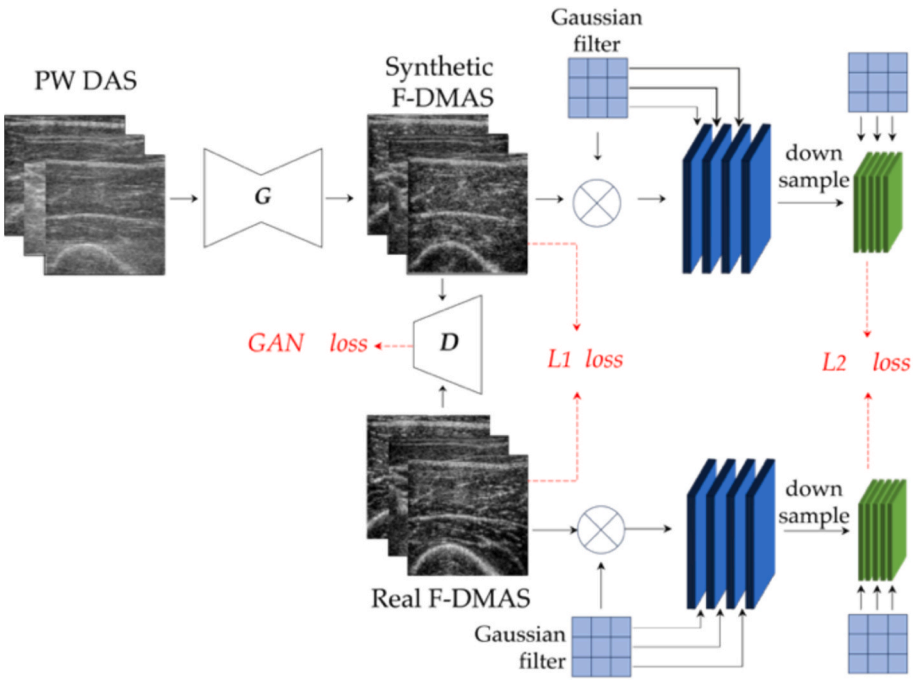

Fig. 2. Pyramid Pixel2Pixel model used to generate focused F-DMAS images from PW DAS images. G: Generator network (Attention-UNet); D: Discriminator network (PatchGAN).

computed after normalizing each image by its mean intensity. This highlights structural differences independently of overall brightness.

2.3.2. Texture features analysis

Texture analysis is valuable in image processing and analysis as it allows for the quantification and characterization of fine spatial details [12]. In this study, texture features were extracted to quantitatively compare the structural similarity between the reference focused F-DMAS images and those generated by the six methods, providing an objective metric for evaluating image-to-image translation performance. Specifically, similarity was assessed by computing the average absolute relative error between the texture parameters of each generated image and the corresponding F-DMAS reference. The absolute relative error is defined as:

$$Error_{ij} = \left| \frac{\left| feature_i - feature_j \right|}{feature_j} \right| \tag{4}$$

where the subscript i refers to one of the six analyzed methods and j to the reference image. Comparing these errors allows verification of how closely the texture parameters of the output images match those of the F-DMAS references. Statistical significance of differences was evaluated using the Mann-Whitney test.

The selected texture features are widely used in clinical radiomics and have been validated for analyzing various ultrasound tissues, providing reliable insights into structural and spatial image properties [11]. Utilizing these features, we aimed to quantify the degree to which GAN-generated images replicate the texture characteristics of the F-DMAS reference.

Texture parameters were estimated in four randomly positioned Regions of Interest (ROIs) with different shapes and dimensions. After initial random positioning within the image, the ROIs were fixed for texture parameter computation across all images. Fig. 3 shows an example of texture feature extraction in the DAS, F-DMAS, and Pyramidal GAN images. 27 texture features were estimated using an open-source Python package (Pyradiomics) [43]. First-order features, second-order Haralick features based on the gray level co-occurrence matrix (GLCM) [44], and second-order Galloway features based on the gray level run length matrix (GLRLM) [45] were computed in the four ROIs. To summarize the results, the texture features computed across the four ROIs were averaged. Statistical analyses were performed to assess whether the error values for texture parameters showed statistically significant differences. For each texture parameter, we compared the error between the method under analysis and F-DMAS, as well as the error between DAS and F-DMAS. Given that the data did not follow a normal distribution, the Wilcoxon signed-rank test was employed for paired samples to evaluate differences in error values.

2.3.3. Contrast improvement index (CII)

To evaluate the contrast enhancement in the generated images, we computed the contrast improvement index (CII). This metric was computed using the input DAS image as the baseline and it hence measures the contrast improvement that is obtained with the analyzed method. The CII metric was preferred over other contrast metrics as it does not require defining one or two ROIs (i.e., defining the target ROI and background ROI), which are instead necessary for the contrast-to-noise ratio and generalized contrast-to-noise-ratio computation [46]. In addition, to better reflect the objective of simulating F-DMAS reconstructions, we also computed the CII using F-DMAS as the reference.

2.3.4. Visual assessment

Clinical specialists' assessment of image quality provides qualitative insights that complement the quantitative metrics used in this study. This evaluation consisted of two key aspects. First, the clinical utility of the generated images was assessed in comparison to the DAS image to determine whether one generative model consistently produced superior images compared to the others. A specialist operator evaluated 28 images generated by the three GAN models for the two subjects in the test set, alongside the original DAS image. The overall contribution of the generated images relative to the DAS image was assessed and categorized as 'Positive' if the GAN-enhanced image offered clear clinical value over the DAS image, 'Neutral' if no additional benefit was observed, and 'Negative' if the quality of the generated image was deemed worse than the DAS image. Furthermore, the GAN-generated

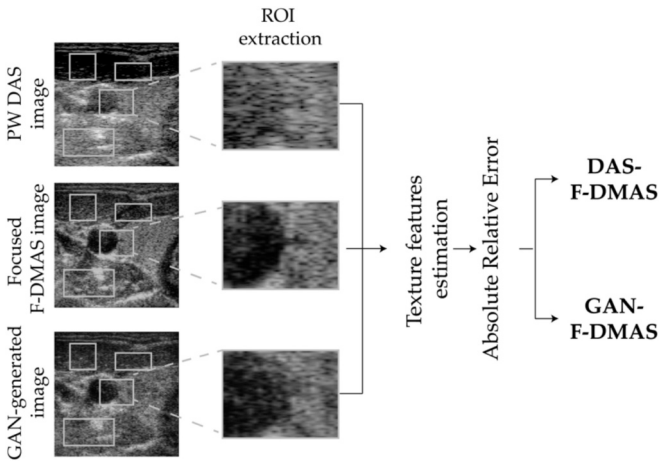

Fig. 3. Pipeline for texture feature similarity quantification. Four Regions of Interest (ROIs) are positioned within the image for estimating texture features. The Absolute Relative Error is computed between the texture features estimated on the analyzed image (i.e., DAS and Pyramidal GAN in this figure), and those estimated on the reference F-DMAS image.

images were ranked from best to worst, with the best image receiving a score of 1 and the worst a score of 3. The mean score and its standard deviation for each GAN model was then computed to assess the relative performance of each model in terms of qualitative image quality. Finally, to further assess perceptual similarity to the target reference, the expert was also asked to evaluate 42 test images containing the DAS, F-DMAS, and the three GAN-generated versions, ranking them from best to worst in terms of overall image quality.

3. Results

Fig. 4 shows an example of the GANs-generated musculoskeletal images compared to DAS, F-DMAS, and the two analyzed traditional image enhancement methods. To compare an estimation of the obtainable lateral resolution with the different methods, the intensity profiles crossing a fascicle within the muscle were drawn and normalized by the maximum intensity. Subsequently, the Full Width Half Maximum (FWHM) was computed, which is commonly employed for resolution analysis. The plane wave DAS image showed a FWHM equal to 37 pixels, or 2.04 mm, whereas the F-DMAS FWHM was equal to 22 pixels, or 1.21 mm. The results obtained using GAN-based methods vary: both Cycle-GAN and Pix2Pix yielded FWHM values comparable to that of F-DMAS, measuring 1.16 mm and 1.38 mm, respectively. In contrast, the Pyramidal method produced a higher FWHM of 2.92 mm. Traditional techniques fell in between, with CLAHE achieving a FWHM of 2.26 mm and HM reaching 1.98 mm. Quantitative results for all methods are summarized in Table 3, which includes RMSE, PSNR, and absolute relative errors on texture features, using F-DMAS as the reference. The Contrast Improvement Index (CII) values are computed with respect to both DAS and F-DMAS. When using DAS as the reference, CII quantifies the contrast enhancement introduced by each method relative to the original DAS reconstruction. When F-DMAS is used as the reference, CII highlights the degree of similarity in contrast achieved by each method relative to the contrast provided by F-DMAS.

3.1. Full reference metrics for image similarity

Table 3 reports the RMSE and PSNR values comparing the six analyzed methods (i.e., DAS, CLAHE, HM, Pix2Pix, Cycle, and Pyramidal) with the F-DMAS reference. The Pyramidal GAN method demonstrates the best performance, achieving the lowest RMSE (0.126 ± 0.008 without normalization, 0.129 ± 0.007 with normalization) and the highest PSNR (18.0 ± 0.6 dB), indicating high image similarity and quality. The other two generative adversarial methods and the traditional methods show similar performance. Among traditional methods, the histogram-matching (HM) approach showed a good performance, with an RMSE of 0.131 ± 0.010 (unchanged by normalization) and a PSNR of 17.7 ± 0.7 dB, outperforming CLAHE, which had the highest RMSE (0.171 ± 0.029 without normalization, 0.137 ± 0.009 with normalization) and the lowest PSNR (15.5 ± 1.4 dB), indicating CLAHE's limited similarity to the target F-DMAS image. In terms of GAN-based methods, the Pix2Pix and Cycle methods produced results comparable to the histogram-matching approach, with PSNR values of

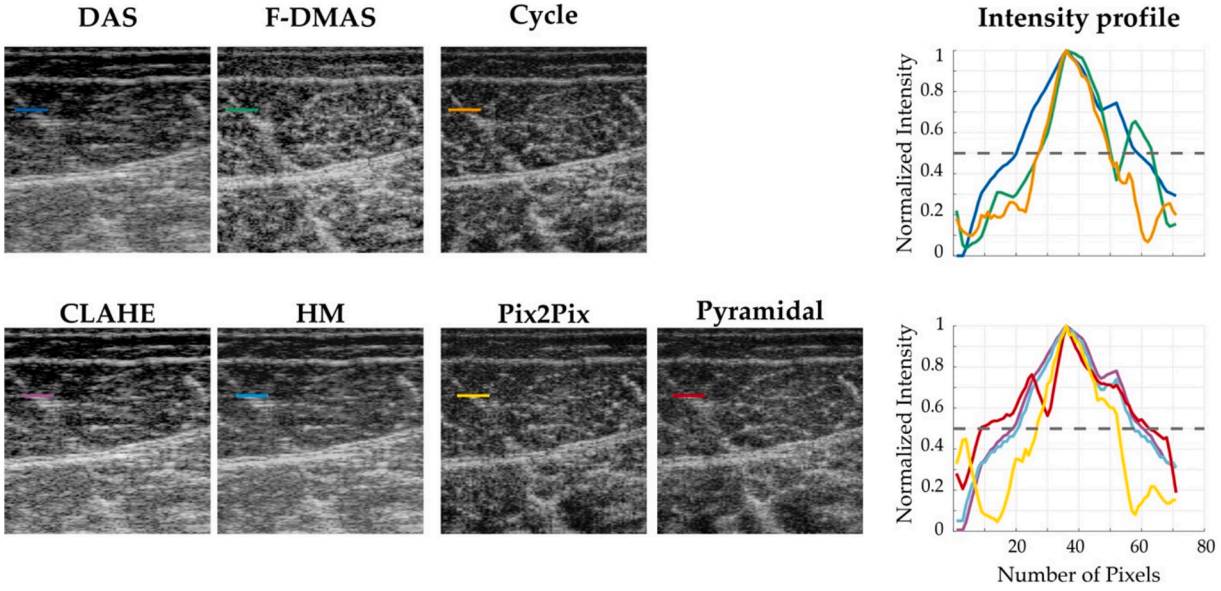

Fig. 4. Examples of a musculoskeletal image highlighting the intensity profile of a fascicle within the muscle. The first row shows the plane wave DAS image along with the F-DMAS image and the output Cycle GAN image. The bottom row shows the other two generative methods (Pix2Pix and Pyramidal) along with the traditional CLAHE and HM methods. The intensity profiles represent the computation of the full width half maximum (FWHM) for each method, which are represented as follows: DAS (blue), F-DMAS (green), Cycle (orange), CLAHE (magenta), HM (cyan), Pix2Pix (yellow), and Pyramidal (red). (For interpretation of the references to colour in this figure legend, the reader is referred to the web version of this article.)

17.6 ± 0.5 dB, 17.7 ± 0.5, and 17.7 ± 0.7 dB, respectively.

3.2. Absolute relative error – Texture analysis

Table 3 presents the absolute relative errors of the texture features relative to the focused F-DMAS image, averaged across the four ROIs. The comparison provides an overall view of how each method performs in terms of texture similarity with the target reference image (i.e., F-DMAS).

The absolute relative errors for texture features indicate that the generative adversarial approaches significantly outperform the original DAS and also the traditional image enhancement methods. Indeed, considering the texture feature validation approach, the Cycle GAN consistently performs the best, when employing both first-order and second-order texture features (0.391 ± 3.428, 0.076 ± 0.103, and 0.097 ± 0.125 for the first-order, Haralick and Galloway features respectively). Overall, the absolute relative errors are systematically lower when comparing generative models (i.e., Pyramidal, Pix2Pix, and Cycle) with traditional contrast-enhancement methods (i.e., CLAHE, HM), underlining how the traditional methods do not transfer texture information as well as the generative models.

When we compared the $Error_{Pyramidal\text{-}FDMAS}$, $Error_{Cycle\text{-}FDMAS}$, $Error_{Pix2Pix\text{-}FDMAS}$ with the $Error_{DAS\text{-}FDMAS}$, all texture parameters showed statistically significant differences (p-value < 0.05), except for the difference variance (Haralick parameter) for the Pyramidal , and the maximum correlation coefficient (Haralick parameter) for the Cycle and Pix2Pix GANs. All Galloway parameters exhibited statistically significant differences. This finding indicates that the texture of the image generated by the three GANs closely emulates the texture of the target F-DMAS image.

3.3. Contrast improvement index (CII) estimation

The CII values for the test set when using the PW DAS image for the reference are reported in the last column of Table 3. The CII values of all methods are higher than 1, indicating an improvement in contrast in the generated image. The Pix2Pix GAN presents the best values among the generative models, equal to 1.297 ± 0.340. As expected, the histogram-matched DAS images and those enhanced with CLAHE also present a CII value (CII_{HMDAS} = 1.294 ± 0.468, CII_{CLAHE} = 1.113 ± 0.067) comparable to the CII values of the generative models. The comparable performance without statistically significant differences among all methods indicates that both traditional and generative approaches effectively enhance image contrast, though generative models offer the additional advantage of texture preservation, as demonstrated by the texture analysis results. Using the F-DMAS image as the reference, the Pix2Pix (0.968 ± 0.054) and CycleGAN (0.963 ± 0.070) models exhibited the highest CII values with the lowest variability, suggesting that these models are not only effective in enhancing image contrast, but also in closely replicating the contrast distribution of the F-DMAS reconstructions.

3.4. Visual assessment

Using the employed image quality metrics, a quantitative difference between the generative models was difficult to observe, making a visual qualitative assessment necessary to further compare the methods. The clinical evaluation consisted of comparing paired images from the test set, which included both the DAS image and the GAN images (Pyramidal, Cycle, and Pix2Pix). The expert clinical evaluation aimed to assess the overall contribution of the GAN-generated images compared to the DAS image. Initially, the comparison among the three GAN models revealed that all three models offered advantages and improvements over the original DAS image. However, the clinical evaluation also indicated that the generated images were often very similar to each other and did not exhibit significant differences from a clinical perspective. In cases where the three GAN models produced nearly identical images, the expert assigned a score of 1 (indicating the best quality) to all three models. This outcome was observed in 18 out of 28 images evaluated. Among the remaining 10 images, the Pyramidal GAN was most frequently identified as producing the best image, receiving a score of 1 in 5 out of these 10 cases. The remaining 5 images had a more balanced distribution of scores across the three models.

Fig. 5 provides an example of carotid and musculoskeletal images generated using the three GAN models and the DAS method, along with the mean scores derived from the qualitative analysis. The figure presents the ranking of the images, with the mean for each GAN model shown in comparison to the DAS image.

In addition to this comparative ranking among GANs and DAS, a further evaluation was conducted to assess how closely the GAN-generated images resemble the F-DMAS target. The expert clinician reviewed 42 test set images that included the DAS (standard 60 dB dynamic range), F-DMAS, and the three GAN-generated outputs, and ranked them from best to worst in terms of perceived image quality. In 78% of the cases, the expert assigned the top score to all GAN and F-DMAS images equally, reporting no discernible difference between them. For the remaining 22% of cases, only one image saw a GAN output ranked above F-DMAS, while in all other instances F-DMAS was preferred. Notably, in these latter cases, the Pyramidal GAN was always ranked immediately after F-DMAS. DAS images were consistently

Table 3
RMSE, PSNR, and Absolute relative error of all texture features and CII values (mean ± standard deviation). Full reference metrics and the Absolute relative errors are computed considering F-DMAS as the reference image. CII values are computed using *input* = DAS and F-DMAS, *output* = F-DMAS, CLAHE, HM, Pix2Pix, CycleGAN and Pyramidal. The best values are reported in bold.

Method		Full reference metrics		Absolute relative errors of all texture features			Contrast metric	
		RMSE ↓	PSNR (dB)↑	First order ↓	Haralick ↓	Galloway ↓	CII ↑ (vs F-DMAS)	CII ↑ (vs DAS)
DAS	w/ N	0.130 ± 0.009	16.0 ± 1.6	1.023 ± 10.798	0.237 ± 0.392	0.765 ± 6.034	0.815 ± 0.249	–
	w/o N	0.161 ± 0.031						
F-DMAS		–	–	–	–	–		**1.343 ± 0.402**
CLAHE	w/ N	0.137 ± 0.009	15.5 ± 1.4	0.917 ± 9.226	0.189 ± 0.342	0.472 ± 4.286	0.892 ± 0.222	1.113 ± 0.067
	w/o N	0.171 ± 0.029						
HM	w/ N	0.131 ± 0.010	17.7 ± 0.7	1.913 ± 26.101	0.201 ± 0.381	0.788 ± 6.714	0.873 ± 0.102	1.294 ± 0.468
	w/o N	0.131 ± 0.010						
Pix2Pix GAN	w/ N	0.129 ± 0.008	17.6 ± 0.5	0.568 ± 5.432	0.087 ± 0.114	0.099 ± 0.151	**0.968 ± 0.054**	1.297 ± 0.340
	w/o N	0.131 ± 0.008						
Cycle GAN	w/ N	0.129 ± 0.007	17.7 ± 0.5	**0.391 ± 3.428**	**0.076 ± 0.103**	**0.097 ± 0.125**	0.963 ± 0.070	1.292 ± 0.341
	w/o N	0.131 ± 0.007						
Pyramidal GAN	w/ N	0.129 ± 0.007	**18.0 ± 0.6**	0.582 ± 5.347	0.108 ± 0.097	0.121 ± 0.135	0.862 ± 0.057	1.156 ± 0.349
	w/o N	**0.126 ± 0.008**						

w/ N and w/o N represent with and without normalization respectively.

ranked as the lowest in quality. These results support the ability of the GAN-based methods to generate images that perceptually mimic the quality and structure of the F-DMAS reconstructions.

Considering that the Pyramidal GAN is most frequently identified as producing the best images, a final evaluation of the robustness of the generated images among different dR values is performed. The first row of Fig. 6 presents a subset of input PW DAS images of the test set obtained using different dR values. The bottom row shows the images generated by Pyramidal GAN model, which were produced by using the corresponding PW DAS images as input. The computed CII values for each image are also shown. As the dR increases, the CII values also increase, particularly peaking at dR = 70 dB. This trend is explained by the inverse relationship between dR and perceived contrast in DAS images: higher dR values result in DAS images with visually reduced contrast between tissue structures. Consequently, when the GAN generates enhanced images from these higher dR inputs, the relative contrast improvement (measured by CII) becomes more pronounced. Notably, the GAN-generated images remain visually consistent across the different dR values, demonstrating the stability and robustness of the model. This consistency indicates that the GAN effectively adapts to different input characteristics while maintaining similar output quality. The results reflect the model's ability to generalize and maintain high-quality outputs even with varying input dynamic ranges.

4. Discussion

In this study, we proposed an innovative approach for ultrasound image enhancement through beamforming domain transfer from PW DAS to focused F-DMAS images. The generative models overcome the main limitation of alternative beamforming methods by mimicking F-DMAS beamforming without the need for accessing raw RF data. One of the key features of the GAN models is its ability to generate focused-mode ultrasound B-mode images from PW images while simultaneously optimizing dynamic range values for each image type [34]. In this study, we focus on the domain transfer from single plane wave to focused wave transmission as a case study, but it is important to underline that there is no inherent limitation to the proposed approach, which could be generalized to cover other transmission modalities. The GANs demonstrate the ability to generalize image generation across the different considered anatomical structures, which are muscular and vascular districts. Moreover, this approach provides an opportunity to overcome the limitation of lacking access to raw RF data in typical clinical ultrasound systems, offering a practical and computationally efficient solution for enhancing image contrast and texture, as demonstrated by the qualitative analysis and CII results. The low computational cost of the GANs makes this method suitable for potential clinical applications, providing clinicians with enhanced image quality to support diagnosis without requiring significant changes to existing ultrasound hardware.

The GAN models demonstrate superior image quality and texture preservation, closely aligning with the F-DMAS gold standard across multiple evaluation metrics. As shown in Table 3, the Pyramidal GAN achieves the lowest RMSE (0.126 ± 0.006) and the highest PSNR (18.0 ± 0.6 dB), outperforming all other methods, including traditional techniques like CLAHE and HM, as well as the other generative models like Pix2Pix and Cycle, but the differences are not statistically significant. The use of different dynamic range values for the input DAS images may present a bias in the computed RMSE values, specifically for the DAS and conventional image enhancement methods (i.e., CLAHE and HM). Further tests were hence done to compensate for amplitude offsets by removing the mean value from the 8-bit images and recalculating the RMSE values. As expected, this normalization reduces all RMSE values (from 0.161 ± 0.031 to 0.130 ± 0.009 for DAS; from 0.131 ± 0.007 to 0.129 ± 0.007 for the Cycle GAN), but the relative performance ranking remains essentially unchanged. This indicates that our conclusions are robust to amplitude variations inherent in ultrasound imaging and again underlines how the RMSE parameter was not relevant for distinguishing between the considered approaches. Moreover, it is important to underline that it is not to be expected that the original DAS and the CLAHE and HM methods present lower RMSE values, as the images are indeed reconstructed using different methods. Still, they presented similar results, underlining also a key limitation of RMSE as a standalone metric in medical imaging. As recent studies have shown, standard full-reference metrics often fail to capture perceptually or diagnostically relevant differences [47]. For this reason, we interpret RMSE alongside visual inspection, texture-based metrics, and other task-specific evaluations.

We therefore further validated the GAN model through contrast and texture analyses. The CII contrast analysis shows that the GAN images

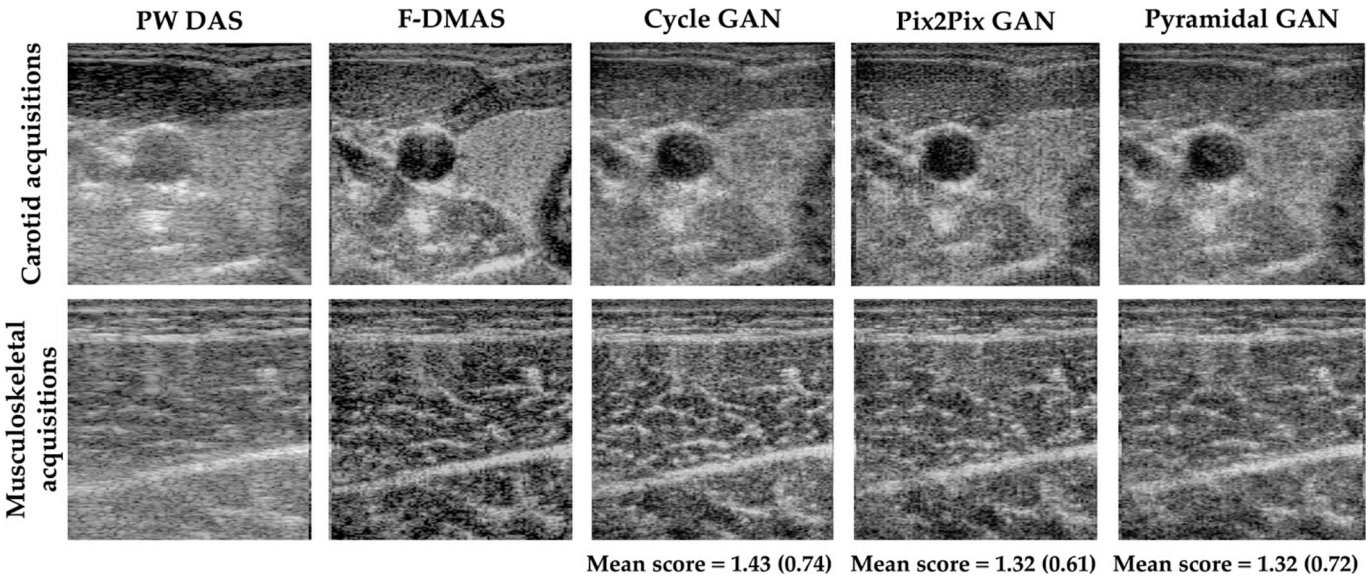

Fig. 5. Example of carotid and musculoskeletal images generated using the three GAN models (Pyramidal, Cycle, and Pix2Pix), F-DMAS and the DAS method. For each image pair, the corresponding qualitative clinical score is shown. The scores represent the ranking of the GAN-generated images, with 1 being the highest score, indicating the best quality, and 3 being the lowest. The mean scores for each GAN model are calculated from the clinical evaluation with the standard deviation shown in parentheses.

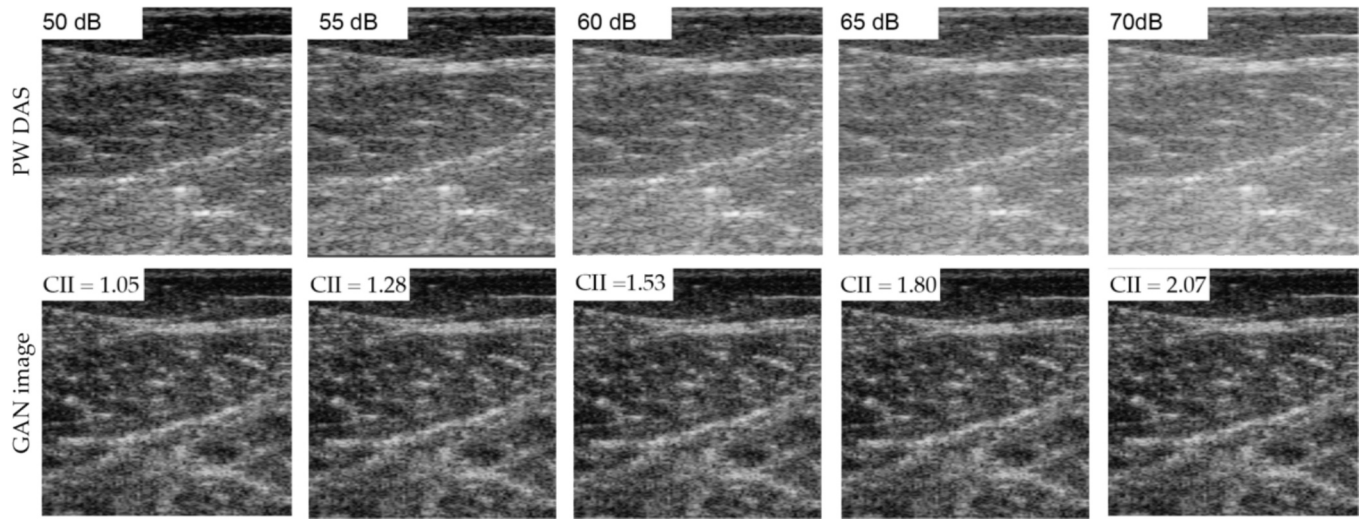

Fig. 6. PW DAS images with different dR values alongside the corresponding Pyramidal GAN-generated image and CII values (test set). The figure shows the same DAS and GAN images generated with varying dR values (from 50 to 70 dB in increments of 5). For each image pair (DAS and GAN), the corresponding CII value is provided.

improve contrast over the DAS image in both training and test sets. The Pix2Pix GAN's contrast enhancement, with an average CII of 1.297 ± 0.340, closely matches the F-DMAS CII of 1.343 ± 0.402. This indicates that this GAN effectively emulates F-DMAS contrast enhancement using PW DAS images in input. Still, the values are similar among all considered methods, both generative and traditional, and no statistically significant differences were observed. As shown in Fig. 2, even at the lowest dR value of 50 dB, the CII remains above 1, showcasing the consistent contrast enhancement achieved and the ability to generate images with enhanced contrast across various dR values. While traditional methods like histogram matching and CLAHE also showed a marked contrast improvement ($CII_{HM} = 1.294 \pm 0.468$, $CII_{CLAHE} = 1.113 \pm 0.067$), they fell short in texture analysis. The absolute relative error of these methods for the first-order and second-order texture features were consistently more similar to those of DAS and higher than those of the generative models (Table 3). As can be noted from Table 3, the absolute relative error of the first-order texture features present high standard deviation values. This is mainly due to two things: (1) one of the considered first-order texture features (i.e., skewness) can present negative values making the crossing zero from negative to positive potentially increase the error magnitude, and (2) a small or negative denominator (i.e., the reference value), which again amplifies the relative error and can produce values greater than one. Moreover, it can also be observed that a similar situation of high standard deviation values is present for the second-order Galloway features, but only for the DAS, CLAHE and HM methods. Investigating this further demonstrated that some images presented texture parameter values (i.e., Long Run Emphasis and Run Variance) that were abnormally high, resulting in large absolute relative error values. This was due mainly to a low dynamic range value (i.e., 50 dB or 55 dB) which presented in some of the considered ROIs a large hypoechoic or isoechoic region which contributed in increasing the long run emphasis and run variance parameters. This was not observed in any of the GAN-produced images. The texture parameter validation analysis demonstrates that, while histogram matching and adaptive contrast enhancement methods indeed enhance contrast, they fail to replicate F-DMAS texture features accurately, as expected. Texture parameters were used here as quantitative metrics to evaluate image similarity between generated and reference images, rather than as direct indicators of containing clinically relevant information. Indeed, our hypothesis is that the F-DMAS image could potentially provide new insight when compared to DAS, but more specifically focused studies are required to evaluate the clinical relevance of the F-DMAS texture, which is out of scope of this present study. It is also important to underline that histogram matching on the target image is not implementable in real inference settings (e.g. when the target F-DMAS image is not available). On the other hand, the GAN images closely match the F-DMAS texture while also providing enhanced contrast, and this is implementable in real inference settings. For this validation analysis, the Cycle GAN consistently produced the best results. These findings are in line with our previous study [17], which highlighted how beamforming methods do influence the ultrasound B-mode texture, which could prove to be crucial in pathology classification; still, further studies are needed to accurately assess these potential differences. Our findings hence underline how, if RF raw data are not available, a generative deep learning model is necessary to effectively transfer texture information and not just enhance contrast or reduce noise.

The clinician's qualitative analysis shows that the images generated by the GANs lead to an overall improvement in clinical assessment. The GAN models provide superior resolution and detail compared to DAS images, particularly for muscular tissues, which enhances clinical visual analysis. Meanwhile, the vascular images provide a better definition of the vessel and its structure. Furthermore, the GAN models specifically improve the dynamic range of DAS images, optimizing clinical evaluation, particularly for vascular images, by generating images with an optimized dR value from any range of 50–70 dB for the input PW DAS image. Additionally, the clinical evaluation revealed no substantial differences among the images generated by the three GANs, as they were often very similar and showed no clinically significant differences.

One potential application of the proposed model is enhancing images acquired in ultrafast (UF) mode. Indeed, in UF ultrasound mode, where PW DAS imaging is commonly used for image acquisition due to its computational and time efficiency, the adversarial methods facilitate the transformation of low-quality UF images into high-quality ones. These generated images closely mimic the texture of focused F-DMAS images while enhancing contrast, which could facilitate fascicle tracking [48].

Despite the promising results, our approach is not without limitations. Although the GAN-based approach does not require raw RF data and operates on pixel-based images, it loses phase information, making it less suitable for ultrafast applications needing precise motion tracking or blood flow detection. Indeed, while methods based on RF data analysis provide precise control over beamforming and theoretical guarantees for contrast enhancement and speckle reduction, GAN-based methods approximate these improvements through training on example

data. This introduces some trade-offs, such as potential biases from the training dataset and limited generalization to underrepresented imaging scenarios. However, the GAN approach offers a practical and effective solution for improving image quality in scenarios where access to raw data is not feasible. Future studies could also explore the generalization of image generation across a wider range of anatomical regions, expanding the dataset and the scope of this method. Additionally, while the choice of pixel dimensions used in this study is consistent with common clinical practices, we acknowledge that pixel dimensions can significantly impact the texture and quality of the generated images. As such, the generalizability of our results across different resolutions remains to be fully explored, and future work should assess how variations may influence the performance of the model, particularly concerning texture representation and overall image quality. Moreover, future research might investigate the generation of ultrasound images similar to those produced by image acquisition methods, such as PW compounding, which offer improved contrast and resolution but still suffer from longer acquisition times than single PW imaging. Future studies could also explore how the GAN approach can be generalized to other beamforming methods to validate its broader applicability in clinical settings. Given the importance of Explainable Artificial Intelligence (XAI) and Uncertainty Quantification (UQ) techniques in enhancing the robustness of AI models [49,50], further investigations could also explore the application of these techniques within the realm of image reconstruction. Moreover, the proposed model can be used in post-processing mode, allowing for the improvement of image quality after acquisition. This approach can improve automatic analysis algorithms, especially for musculoskeletal images, where enhancing image quality is crucial for better quantitative analysis of tendon abnormalities [51] and for assessing muscle mass and structure changes in patients with steroid myopathy [52].

Additional information

This work was supported in part by one of the calls under the Photonics Public Private Partnership (PPP): H2020-ICT-2020-2 with Grant Agreement ID 101016964 (REAP).

Ethics approval

The study was approved by the local ethics committee (n. 24780/2022, approval issued on 19/07/2022).

Patient consent

Written informed consent was provided by all patients before the procedure.

CRediT authorship contribution statement

Silvia Seoni: Formal analysis, Methodology, Writing – original draft, Data curation, Investigation. **Massimo Salvi:** Software, Conceptualization, Writing – review & editing, Investigation, Methodology, Validation, Formal analysis. **Giulia Matrone:** Visualization, Methodology, Writing – review & editing. **Francesco Lapia:** Validation, Writing – review & editing. **Chiara Busso:** Validation, Writing – review & editing. **Marco A. Minetto:** Validation, Writing – review & editing. **Kristen M. Meiburger:** Writing – review & editing, Methodology, Conceptualization, Supervision, Funding acquisition, Visualization, Investigation, Project administration, Formal analysis.

Declaration of competing interest

The authors declare that they have no known competing financial interests or personal relationships that could have appeared to influence the work reported in this paper.

Data availability

The dataset and code are available on Mendeley Data: Seoni, Silvia; Salvi, Massimo; Matrone, Giulia; Lapia, Francesco; Busso, Chiara; Minetto, Marco A.; Meiburger, Kristen M. (2025), "Dataset and codes of the paper "Adversarial learning for beamforming domain transfer in ultrasound medical imaging", Mendeley Data, V1, doi: 10.17632/4yw3pbp4tf.1.

References

[1] A. Carovac, F. Smajlovic, dzelaludin Junuzovic, Application of ultrasound in medicine, Medicine Review | AIM, vol. 19, no. 3, pp. 168–171, 2011, doi: 10.5455/aim.2011.19.168-171.
[2] J. Hli, K.R. Erikson, F.J. Fry, J.P. Jones, Ultrasound in medicine-a review, no. 3, pp. 144–170.
[3] E. Sassaroli, C. Crake, A. Scorza, D.S. Kim, M.A. Park, Image quality evaluation of ultrasound imaging systems: advanced B-modes, J. Appl. Clin. Med. Phys. 20 (3) (Mar. 2019) 115–124, https://doi.org/10.1002/acm2.12544.
[4] T.M. Kolb, J. Lichy, J.H. Newhouse, Comparison of the performance of screening mammography, physical examination, and breast US and evaluation of factors that influence them: an analysis of 27,825 Patient Evaluations1', https://doi.org/10.1148/radiol.2251011667, vol. 225, no. 1, pp. 165–175, Oct. 2002, doi: 10.1148/RADIOL.2251011667.
[5] G. Matrone, A.S. Savoia, G. Caliano, G. Magenes, The delay multiply and sum beamforming algorithm in ultrasound B-mode medical imaging, IEEE Trans. Med. Imaging 34 (4) (2015) 940–949, https://doi.org/10.1109/TMI.2014.2371235.
[6] K. W. Hollman, K. W. Rigby, and M. O. Donnell, 'Coherence Factor', pp. 1257–1260, 1999.
[7] P.C. Li, M.L. Li, Adaptive imaging using the generalized coherence factor, 2003. doi: 10.1109/TUFFC.2003.1182117.
[8] J. Camacho, M. Parrilla, C. Fritsch, Phase coherence imaging, IEEE Trans. Ultrason. Ferroelectr. Freq. Control 56 (5) (2009) 958–974, https://doi.org/10.1109/TUFFC.2009.1128.
[9] J.F. Synnevåg, A. Austeng, S. Holm, Benefits of minimum-variance beamforming in medical ultrasound imaging, IEEE Trans. Ultrason. Ferroelectr. Freq. Control 56 (9) (Sep. 2009) 1868–1879, https://doi.org/10.1109/TUFFC.2009.1263.
[10] M.A. Lediju, G. E. Trahey, B.C. Byram, J.J. Dahl, 'Short-lag spatial coherence of backscattered echoes: imaging characteristics', doi: 10.1109/TUFFC.
[11] M.K. Ghalati, A. Nunes, H. Ferreira, P. Serranho, R. Bernardes, Texture analysis and its applications in biomedical imaging: a survey, IEEE Rev. Biomed. Eng. 15 (2022) 222–246, https://doi.org/10.1109/RBME.2021.3115703.
[12] F. Molinari, C. Caresio, U.R. Acharya, M.R.K. Mookiah, M.A. Minetto, Advances in quantitative muscle ultrasonography using texture analysis of ultrasound images, Ultrasound Med. Biol. 41 (9) (2015) 2520–2532, https://doi.org/10.1016/j.ultrasmedbio.2015.04.021.
[13] S.S.D. Xu, C.C. Chang, C.T. Su, P.Q. Phu, Classification of liver diseases based on ultrasound image texture features, Appl. Sci. 9(2) (2019) 342, doi: 10.3390/APP9020342.
[14] K. Sujatha et al., Screening and early identification of microcalcifications in breast using texture-based ANFIS classification, Wearable and Implantable Medical Devices, pp. 115–140, Jan. 2020, doi: 10.1016/B978-0-12-815369-7.00005-7.
[15] U.R. Acharya, et al., Atherosclerotic risk stratification strategy for carotid arteries using texture-based features, Ultrasound Med. Biol. 38 (6) (2012) 899–915, https://doi.org/10.1016/J.ULTRASMEDBIO.2012.01.015.
[16] M.A. Alqahtani, D.P. Coleman, N.D. Pugh, L.D.M. Nokes, Tissue characterization: influence of ultrasound setting on texture features in vivo, in: 2010 International Conference on Medical Image Analysis and Clinical Application, MIACA 2010, no. 4 cm, pp. 63–66, 2010, doi: 10.1109/MIACA.2010.5528423.
[17] S. Seoni, G. Matrone, K.M. Meiburger, Robustness analysis of texture features with different beamforming techniques. In 2020 IEEE International Ultrasonics Symposium (IUS) (pp. 1 - 4). IEEE.
[18] S. Khan, J. Huh, J.C. Ye, Adaptive and compressive beamforming using deep learning for medical ultrasound, IEEE Trans. Ultrason. Ferroelectr. Freq. Control 67 (8) (2020) 1558–1572, https://doi.org/10.1109/TUFFC.2020.2977202.
[19] A.C. Luchies, B.C. Byram, Deep neural networks for ultrasound beamforming, IEEE Trans. Med. Imaging 37 (9) (2018) 2010–2021, https://doi.org/10.1109/TMI.2018.2809641.
[20] A.A. Nair, K.N. Washington, T.D. Tran, A. Reiter, M.A. Lediju Bell, Deep learning to obtain simultaneous image and segmentation outputs from a single input of raw ultrasound channel data, IEEE Trans. Ultrason. Ferroelectr. Freq. Control 67 (12) (2020) 2493–2509, https://doi.org/10.1109/TUFFC.2020.2993779.
[21] B. Luijten et al., Deep learning for fast adaptive beamforming, ICASSP, IEEE International Conference on Acoustics, Speech and Signal Processing - Proceedings, vol. 2019-May, pp. 1333–1337, 2019, doi: 10.1109/ICASSP.2019.8683478.
[22] B. Luijten, et al., Adaptive ultrasound beamforming using deep learning, IEEE Trans. Med. Imaging 39 (12) (2020) 3967–3978, https://doi.org/10.1109/TMI.2020.3008537.
[23] A.A. Nair, T.D. Tran, A. Reiter, M.A.L. Bell, A generative adversarial neural network for beamforming ultrasound images: invited presentation, in: 2019 53rd Annual Conference on Information Sciences and Systems, CISS 2019, pp. 1–6, 2019, doi: 10.1109/CISS.2019.8692835.

[24] S. Seoni, M. Salvi, G. Matrone, K.M. Meiburger, Ultrasound image beamforming optimization using a generative adversarial network, IEEE International Ultrasonics Symposium, IUS IEEE Computer Society (2022), https://doi.org/10.1109/IUS54386.2022.9957306.
[25] X. He et al., Deep attentional GAN-based high-resolution ultrasound imaging, SPIE-Intl Soc Optical Eng, Mar. 2020, p. 10. doi: 10.1117/12.2549556.
[26] M. Escobar, A. Castillo, A. Romero, P. Arbeláez, 'UltraGAN: ultrasound enhancement through adversarial generation'. [Online]. Available: https://github.com/BCV-Uniandes/UltraGAN.
[27] Z. Zhou, Y. Wang, Y. Guo, Y. Qi, J. Yu, Image quality improvement of hand-held ultrasound devices with a two-stage generative adversarial network, IEEE Trans. Biomed. Eng. 67 (1) (Jan. 2020) 298–311, https://doi.org/10.1109/TBME.2019.2912986.
[28] Z. Zhou, Y. Guo, Y. Wang, Ultrasound deep beamforming using a multiconstrained hybrid generative adversarial network, Med. Image Anal. 71 (Jul. 2021) 102086, https://doi.org/10.1016/J.MEDIA.2021.102086.
[29] H.G. Khor, G. Ning, X. Zhang, H. Liao, Ultrasound speckle reduction using wavelet-based generative adversarial network, IEEE J. Biomed. Health Inform. 26 (7) (Jul. 2022) 3080–3091, https://doi.org/10.1109/JBHI.2022.3144628.
[30] E. Bosco, E. Spairani, E. Toffali, V. Meacci, A. Ramalli, G. Matrone, A deep learning approach for beamforming and contrast enhancement of ultrasound images in monostatic synthetic aperture imaging: a proof-of-concept, IEEE Open J Eng Med Biol 5 (2024) 376–382, https://doi.org/10.1109/OJEMB.2024.3401098.
[31] D. Hyun, et al., Deep learning for ultrasound image formation: CUBDL evaluation framework and open datasets, IEEE Trans. Ultrason. Ferroelectr. Freq. Control 68 (12) (Dec. 2021) 3466–3483, https://doi.org/10.1109/TUFFC.2021.3094849.
[32] H. Liebgott, A. Rodriguez-Molares, F. Cervenansky, J.A. Jensen, O. Bernard, Plane-wave imaging challenge in medical ultrasound, IEEE International Ultrasonics Symposium, IUS, vol. 2016-November, Nov. 2016, doi: 10.1109/ULTSYM.2016.7728908.
[33] D. Xiao, A.C.H. Yu, Beamforming-integrated neural networks for ultrasound imaging, Ultrasonics 145 (Jan. 2025) 107474, https://doi.org/10.1016/J.ULTRAS.2024.107474.
[34] K.M. Meiburger, S. Seoni, G. Matrone, Automatic dynamic range estimation for ultrasound image visualization and processing, IEEE Int. Ultrason. Symp. IUS 2 (2020) 2–5.
[35] A. Rodriguez-Molares, O.M.H. Rindal, O. Bernard, H. Liebgott, A. Austeng, L. Lovstakken, 'The ultrasound toolbox', IEEE Int. Ultrason. Sympos. IUS, Oct. 2017, doi: 10.1109/ULTSYM.2017.8092026.
[36] P. Isola, J. Y. Zhu, T. Zhou, A. A. Efros, 'Image-to-image translation with conditional adversarial networks', in: Proceedings - 30th IEEE Conference on Computer Vision and Pattern Recognition, CVPR 2017, vol. 2017-January, pp. 5967–5976, Nov. 2017, doi: 10.1109/CVPR.2017.632.
[37] J. Y. Zhu, T. Park, P. Isola, A.A. Efros, Unpaired image-to-image translation using cycle-consistent adversarial networks, in: Proceedings of the IEEE International Conference on Computer Vision, vol. 2017-October, pp. 2242–2251, Dec. 2017, doi: 10.1109/ICCV.2017.244.
[38] H. Yin, J. Xiao, H. Chen, CSPA-GAN: a cross-scale pyramid attention GAN for Infrared and visible image fusion, IEEE Trans. Instrum. Meas. 72 (2023), https://doi.org/10.1109/TIM.2023.3317932.
[39] A.M. Reza, Realization of the contrast limited adaptive histogram equalization (CLAHE) for real-time image enhancement, J. VLSI Signal Process. Syst. Signal Image Video Technol. 38 (1) (Aug. 2004) 35–44, https://doi.org/10.1023/B:VLSI.0000028532.53893.82/METRICS.
[40] S.S. Bagade, V.K. Shandilya, A. Proffessor, Use of histogram equalization in image processing for image enhancement.
[41] M.K. Choong, R. Logeswaran, M. Bister, Improving diagnostic quality of MR images through controlled lossy compression using SPIHT, J. Med. Syst. 30 (3) (Jun. 2006) 139–143, https://doi.org/10.1007/S10916-005-8374-4/METRICS.
[42] A.J. Dinu, R. Ganesan, A.A. Kebede, B. Veerasamy, Performance analysis and comparison of medical image compression techniques, in: 2016 International Conference on Control Instrumentation Communication and Computational Technologies, ICCICCT 2016, pp. 738–745, 2017, doi: 10.1109/ICCICCT.2016.7988050.
[43] J.J.M. Van Griethuysen, et al., Computational radiomics system to decode the radiographic phenotype, Can. Res. 77 (21) (Nov. 2017) e104.
[44] R.M. Haralick, I. Dinstein, K. Shanmugam, Textural features for image classification, IEEE Trans. Syst. Man Cybern. SMC (1973) 610–621, https://doi.org/10.1109/TSMC.1973.4309314.
[45] M.M. Galloway, Texture analysis using gray level run lengths, Comput. Graphics Image Process. 4 (2) (1975) 172–179, https://doi.org/10.1016/s0146-664x(75)80008-6.
[46] A. Rodriguez-Molares, et al., The generalized contrast-to-noise ratio: a formal definition for lesion detectability, IEEE Trans. Ultrason. Ferroelectr. Freq. Control 67 (4) (2020) 745–759, https://doi.org/10.1109/TUFFC.2019.2956855.
[47] A. Breger, et al., A Study of why we need to reassess full reference image quality assessment with medical images, J. Imag. Inform. Med. 2025 (Mar. 2025) 1–26, https://doi.org/10.1007/S10278-025-01462-1.
[48] J.G. Gillett, R.S. Barrett, G.A. Lichtwark, Reliability and accuracy of an automated tracking algorithm to measure controlled passive and active muscle fascicle length changes from ultrasound, Comput. Methods Biomech. Biomed. Engin. 16 (6) (2013) 678–687, https://doi.org/10.1080/10255842.2011.633516.
[49] S. Seoni, et al., Application of uncertainty quantification to artificial intelligence in healthcare: a review of last decade (2013-2023), Comput. Biol. Med. (2023), https://doi.org/10.1016/j.compbiomed.2023.107441.
[50] H.W. Loh, C.P. Ooi, S. Seoni, P.D. Barua, F. Molinari, U.R. Acharya, Application of explainable artificial intelligence for healthcare: a systematic review of the last decade (2011–2022)', Nov. 01, 2022, Elsevier Ireland Ltd. doi: 10.1016/j.cmpb.2022.107161.
[51] K.M. Meiburger et al., Quantitative analysis of patellar tendon abnormality in asymptomatic professional "Pallapugno" players: a texture-based ultrasound approach, Appl. Sci. 8(5) (2018) 660, doi: 10.3390/APP8050660.
[52] M.A. Minetto et al., Ultrasound-based detection of glucocorticoid-induced impairments of muscle mass and structure in Cushing's disease 42 (2019) 757–768, doi: 10.1007/s40618-018-0979-9.